Computers and Geotechnics 186 (2025) 107379

Contents lists available at ScienceDirect

Computers and Geotechnics

journal homepage: www.elsevier.com/locate/compgeo

Research paper

Integration of critical state theory into a micromechanical model for granular materials accounting for fabric evolution

Hai-Lin Wang [a,b], Xiaoqiang Gu [a,*], Zhen-Yu Yin [b], Chao-Fa Zhao [c]

[a] Department of Geotechnical Engineering, College of Civil Engineering, Tongji University, Shanghai, China
[b] Department of Civil and Environmental Engineering, The Hong Kong Polytechnic University, Hong Kong, China
[c] Department of Civil Engineering, College of Civil Engineering and Architecture, Zhejiang University, Hangzhou, China

ARTICLE INFO

Keywords:
Granular materials
Constitutive model
Micromechanics
Multiscale
Critical state
Fabric anisotropy

ABSTRACT

In geotechnical engineering, the development of efficient and accurate constitutive models for granular soils is crucial. The micromechanical models have gained much attention for their capacity to account for particle-scale interactions and fabric anisotropy, while requiring far less computational resources compared to discrete element method. Various micromechanical models have been proposed in the literature, but none of them have been conclusively shown to agree with the critical state theory given theoretical proof, despite the authors described that their models "approximately" reach the critical state. This paper modifies the previous CHY micromechanical model that is compatible with the critical state theory based on the assumption that the microscopic force–dilatancy relationship should align with the macroscopic stress–dilatancy relationship. Moreover, under the framework of the CHY model, the fabric anisotropy can be easily considered and the anisotropic critical state can be achieved with the introduction of the fabric evolution law. The model is calibrated using drained and undrained triaxial experiments and the results show that the model reliably replicates the mechanical behaviors of granular materials under both drained and undrained conditions. The compatibility of the model with the critical state theory is verified at both macroscopic and microscopic scales.

1. Introduction

One of the most important tasks in the field of geotechnical engineering is to develop an efficient and accurate constitutive model for granular materials. In the last several decades, granular materials have been considered as continuous media with the development of continuum mechanics. Based on the continuum mechanics, phenomenological constitutive models have been widely used to describe the mechanical behavior of granular materials. Due to the discrete nature of the granular materials, an increasing number of difficulties have been encountered in the application of the phenomenological constitutive models, especially in the description of the particle-scale behaviors. To overcome the difficulties, the discrete element method (DEM) (Cundall and Strack, 1979) has been developed to consider these behaviors at the particle scale by modeling the interactions between individual particles. However, DEM is computationally expensive and time-consuming due to the large number of particles and the complex contact interactions.

The micromechanical models have received much more attention in the last several decades (Walton, 1987; Jenkins, 1988; Rothenburg and Bathurst, 1989; Wan and Guo, 2001; Li and Dafalias, 2002; Suiker and Chang, 2004; Chang and Hicher, 2005; Darve and Nicot, 2005b,a; Nicot and Darve, 2011; Xiong et al., 2017). With the consideration of the force–displacement relationship at the contact level and the macroscopic behaviors retrieved from the average of the local contacts based on the Love–Weber formula (Love, 1927; Weber, 1966), the micromechanical models can provide a better understanding of the particle-scale behaviors than the continuum models and the computational cost is much lower than the DEM simulations. Instead of describing the status of every particle at the microscale, the micromechanical model averages the microscopic quantities at contact in specific directions to derive macroscopic behaviors in a statistical manner. This approach proves to be significantly more efficient than the DEM simulations. However, since we cannot determine the status of every particle, the particle arrangement that is critical to macroscopic behaviors like dilatancy cannot be determined. To account for the macroscopic behaviors, Chang and Hicher (2005) introduced a micromechanical model that incorporates an advanced contact law similar to a macroscopic phenomenological model. This approach makes the model acts like a

* Corresponding author.
E-mail addresses: wanghailin@tongji.edu.cn (H.-L. Wang), guxiaoqiang@tongji.edu.cn (X. Gu), zhenyu.yin@polyu.edu.hk (Z.-Y. Yin), chaofa.zhao@zju.edu.cn (C.-F. Zhao).

https://doi.org/10.1016/j.compgeo.2025.107379
Received 30 December 2024; Received in revised form 7 May 2025; Accepted 26 May 2025
Available online 12 June 2025
0266-352X/

combination of several macroscopic models, with the added ability to account for fabric anisotropy by adjusting directional weights within the summation in the averaging operator. This model (noted as CHY model) has been extended and proved its accuracy in clay (Chang et al., 2009; Yin and Chang, 2009), sand–silt mixture (Yin et al., 2014), anisotropic soils (Chang and Yin, 2010; Yin et al., 2010), unsaturated soils (Hicher and Chang, 2007; Zhao et al., 2017) and instability of sands (Chang et al., 2011; Zhao et al., 2018b). Nicot and Darve (2011) introduced an alternative method (H-microdirectional model) that integrates particle arrangements into the micromechanical model by introducing a basic element composed of several particles, where microscopic quantities such as forces and displacements are applied. A simple Coulomb contact law is used to define the relationship between the contact force and displacement. Serving as an intermediate approach between a micromechanical model that considers only two-particle interactions and DEM, this ability of the model to simulate complex behaviors remains uncertain due to the strong assumptions for the basic element.

Achieving the critical state is essential for developing a micromechanical model. However, none of the models mentioned above are proved to be compatible with the critical state theory. Although researchers (Nicot et al., 2005; Chang and Hicher, 2005; Xiong et al., 2017; Zhao and Kruyt, 2020) claimed that their proposed micromechanical models “approximately” converged to the critical state based on the simulation results. However, no theoretical proof was provided for their statements. How to propose a micromechanical model compatible with the critical state theory, for example based on the CHY model, should be clarified. It was discovered that the incompatibility of the original CHY model with the critical state theory is attributed to the averaging strain tensor. Since the CHY model does not account for the actual particle arrangements, a force–dilatancy relationship is incorporated into the normal contact force–displacement relationship. To ensure that the macroscopic stress–dilatancy relationship aligns with the microscopic force–dilatancy relationship, the averaging strain tensor must fulfill the requirement that zero contact normal displacement leads to zero volumetric strain. However, the averaging strain tensor derived from Liao et al. (1997) does not meet this requirement. Therefore, in this paper, a new averaging strain formulation is proposed to ensure that the model is compatible with the critical state theory.

Fabric anisotropy is another important aspect in granular materials. Li and Dafalias (2012) proposed the framework of anisotropic critical state theory where the fabric anisotropy is considered as another condition for the critical state. Fabric anisotropy has been introduced in the dilatancy state line, yield function and plastic potential function (Papadimitriou et al., 2019; Petalas et al., 2019; Gao et al., 2014; Gao and Zhao, 2017) to consider the effect of fabric anisotropy on the critical state.

This paper aims to propose a micromechanical model that integrates the critical state theory while accounting for fabric anisotropy. It begins by introducing the original CHY model and subsequently describes modifications to incorporate fabric anisotropy and critical state theory. The proposed model is calibrated with data from drained and undrained triaxial experiments on sands. The simulation results are then compared with experimental data to validate the accuracy of the model in capturing the mechanical behavior of granular materials at both macroscopic and microscopic scales.

2. Introduction of the original CHY model

The CHY micromechanical model was initially proposed by Chang and Hicher (2005) for sand, and later extended to simulate unsaturated soils (Hicher and Chang, 2007; Zhao et al., 2017, 2019), clay (Chang et al., 2009) and sand–silt mixture (Yin et al., 2014). Further extensions were made to consider the effect of inherent anisotropy (Chang and Yin, 2010; Yin et al., 2010) and instability (Chang et al., 2011; Zhao et al., 2018b). It was also integrated into the finite element software ABAQUS by using the user-defined material subroutine (Zhao et al., 2018a) to solve boundary value problems. The following sections present the micromechanical framework of the CHY model, including the inter-particle contact law, macro–micro integration, consideration of fabric anisotropy, and global mixed load control.

2.1. Inter-particle contact law

The inter-particle contact law is used to describe the force–displacement relationship at the contact level.

2.1.1. Elasticity

A nonlinear elastic model is used to describe the elastic behavior of the contact:

$$\mathrm{d}\mathbf{f}_i^c = \mathbf{k}_{ij}^{e,c}\mathrm{d}\mathbf{u}_j^c, \mathbf{k}_{ij}^{e,c} = \mathrm{diag}([k_n^c, k_r^c, k_r^c]) \tag{1}$$

where $\mathbf{f}_i^c$ is the contact force, $\mathbf{u}_j^c$ is the contact displacement, $\mathbf{k}_{ij}^{e,c}$ is the elastic stiffness matrix, and $\mathrm{diag}(\cdot)$ is the diagonal function that constructs a diagonal matrix from a vector. The normal stiffness k_n^c and tangential stiffness k_r^c are expressed as:

$$k_n^c = k_{n0}^c\left(\frac{f_n^c}{f_{ref}}\right)^{n_e}, k_r^c = k_{rR}k_n^c \tag{2}$$

where f_n^c is the normal contact force, k_{n0}^c is the reference normal stiffness, f_{ref} is the reference contact force, n_e is the elastic exponent, and k_{rR} is the ratio of the tangential stiffness to the normal stiffness. According to Chang and Liao (1994), the Young's modulus E, shear modulus G, and Poisson's ratio ν for isotropic materials can be calculated as:

$$\begin{aligned}
E &= \frac{10k_n^c}{r\upsilon}\frac{k_{rR}}{2+3k_{rR}}\\
G &= \frac{5k_n^c}{r\upsilon}\frac{k_{rR}}{3+2k_{rR}}\\
\nu &= \frac{1-k_{rR}}{2+3k_{rR}}
\end{aligned} \tag{3}$$

where $\upsilon = (3V)/(2Nr^3)$.

2.1.2. Plasticity

A Coulomb-type frictional contact law is used to describe the plastic behavior with the yield function F expressed as:

$$\begin{aligned}
&F = f_r^c - f_n^c\frac{k_p^c\tan\phi_p u_r^{p,c}}{f_n^c\tan\phi_p + k_p^c u_r^{p,c}}, k_p^c = k_{pR}k_n^c, f_r^c = \sqrt{(f_s^c)^2 + (f_t^c)^2},\\
&u_r^{p,c} = \sqrt{(u_s^{p,c})^2 + (u_t^{p,c})^2}
\end{aligned} \tag{4}$$

where f_s^c and f_t^c are the shear contact forces, $u_s^{p,c}$ and $u_t^{p,c}$ are the plastic shear displacements, and k_{pR} is a material constant. ϕ_p is the peak friction angle which is a function of the friction angle accounting for the interlocking effect:

$$\tan\phi_p = \left(\frac{e_c}{e}\right)^{n_p}\tan\phi \tag{5}$$

where e_c is the critical state void ratio, e is the void ratio, and n_p is the interlocking exponent, ϕ is the critical friction angle. The critical state line is expressed as:

$$e_c = e_{ref} - \lambda\left(\frac{p'}{p_a}\right)^{\xi} \tag{6}$$

where e_{ref} is the reference void ratio, p' is the mean effective stress, p_a is the atmospheric pressure, and λ is the slope of critical state line. A dilatancy law is defined as:

$$D = \frac{\mathrm{d}u_n^{p,c}}{\mathrm{d}u_r^{p,c}} = A_d \left(\tan\phi_d - \frac{f_r^c}{f_n^c} \right) \tag{7}$$

where A_d is a dilatancy material constant, the dilatancy friction angle ϕ_d is defined as:

$$\tan\phi_d = \left(\frac{e}{e_c} \right)^{n_d} \tan\phi \tag{8}$$

where n_d is the dilatancy exponent. The void ratio is updated as:

$$\mathrm{d}e = -\mathrm{d}\varepsilon_v (1 + e_0) \tag{9}$$

where $\mathrm{d}\varepsilon_v$ is the volumetric strain increment, e_0 is the initial void ratio.

2.1.3. Transformation of the local and global quantities

The inter-particle contact law is defined at the local coordinates (n, s, t) whereas the stress–strain relationship is defined at the global coordinates (x, y, z). Assume γ is the azimuthal angle between the contact normal and x axis and β is the azimuthal angle between the projection of the contact normal in the yz plane and y axis, any local quantity ($\mathbf{Q}_{\mathrm{local}}$) can be transformed in the global coordinates ($\mathbf{Q}_{\mathrm{global}}$) with the following rotation matrix (Iyanaga and Kawada, 1993):

$$\mathbf{Q}_{\mathrm{local}} = \mathbf{R}\mathbf{Q}_{\mathrm{global}}, \mathbf{Q}_{\mathrm{global}} = \mathbf{R}^{-1}\mathbf{Q}_{\mathrm{local}} = \mathbf{R}^{\mathrm{T}}\mathbf{Q}_{\mathrm{local}}$$

$$\mathbf{R} = \begin{bmatrix} \cos\gamma & \sin\gamma\cos\beta & \sin\gamma\sin\beta \\ -\sin\gamma & \cos\gamma\cos\beta & \cos\gamma\sin\beta \\ 0 & -\sin\beta & \cos\beta \end{bmatrix} \tag{10}$$

2.2. Macro–micro integration

The macro–micro integration relates the macroscopic variables to the microscopic variables. The CHY micromechanical model adopts a best-fit static hypothesis that the mean displacement field is the best-fit of the actual displacement field. Based on the best-fit hypothesis, the local contact displacements can be averaged to the global strain:

$$\mathrm{d}\varepsilon_{ij} = \frac{1}{V}\sum_{c=1}^{N} \mathrm{d}\mathbf{u}_i^c \mathbf{l}_n^c \mathbf{A}_{jn}, \mathbf{A}_{jn} = \left(\frac{1}{V}\sum_{c=1}^{N} \mathbf{l}_j^c \mathbf{l}_n^c \right)^{-1} \tag{11}$$

where $\mathbf{u}_i^c$ is the contact displacement, $\mathbf{l}_j^c$ and $\mathbf{l}_n^c$ are branch vectors, N/V is number of contacts per unit volume, and $\mathbf{A}_{jn}$ is the fabric tensor. The relationship between the local contact forces and the global stress is given by the Love–Weber formula (Love, 1927; Weber, 1966):

$$\boldsymbol{\sigma}_{ij} = \frac{1}{V}\sum_{c=1}^{N} \mathbf{f}_i^c \mathbf{l}_j^c \tag{12}$$

Combining Eqs. (11) and (12), the global stress can be localized to the local contact forces (Liao et al., 1997):

$$\mathrm{d}\mathbf{f}_i^c = \mathrm{d}\boldsymbol{\sigma}_{ij} \mathbf{l}_n^c \mathbf{A}_{jn} \tag{13}$$

Combining Eqs. (1), (11), and (13), the stress–strain relationship can be obtained (Hicher and Chang, 2005):

$$\mathrm{d}\varepsilon_{ij} = \mathbf{S}_{ijkl}\mathrm{d}\boldsymbol{\sigma}_{kl}, \mathbf{S}_{ijkl} = \frac{1}{V}\sum_{c=1}^{N} \left(\mathbf{k}_{jl}^c \right)^{-1} \mathbf{l}_m^c \mathbf{l}_n^c \mathbf{A}_{mi}\mathbf{A}_{nk} \tag{14}$$

where $\mathbf{S}_{ijkl}$ is the elastic compliance tensor.

2.3. Consideration of the fabric anisotropy

The fabric anisotropy can be easily considered in the CHY model by adjusting the directional weights within the summation in the averaging operator. According to the definition, the fabric tensor $\mathbf{F}_{ij}$ can be related to the fabric tensor $\mathbf{A}_{ij}$ shown in Eq. (11) by the following equation:

$$\left(\mathbf{A}_{ij} \right)^{-1} = \frac{1}{V}\sum_{c=1}^{N} \mathbf{l}_j^c \mathbf{l}_n^c = 2r \cdot 2r \cdot \frac{N}{V} \left(\frac{1}{N}\sum_{c=1}^{N} \mathbf{n}_i^c \mathbf{n}_j^c \right)$$

$$= 4r^2 \frac{N}{V} \mathbf{N}_{ij} = 4r^2 \frac{N}{V} \left(\frac{2}{15}\mathbf{F}_{ij} + \frac{1}{3}\mathbf{I}_{ij} \right) \tag{15}$$

where r is the particle radius, $\mathbf{I}_{ij}$ is the identity tensor.

Two types of the fabric evolution laws exist in the literature: the stress-rate driven evolution law (Wan and Guo, 2004; Yang, 2014; Hu et al., 2021) and the strain-rate driven evolution law (Sun and Sundaresan, 2011; Li and Dafalias, 2012; Tian and Yao, 2018; Zhao and Kruyt, 2020; Wang et al., 2020). In this paper, we adopt the strain-rate-driven evolution law proposed by Zhao and Kruyt (2020), as it has been integrated into the CHY micromechanical model. The expression for the evolution law of the fabric tensor is as follows:

$$\mathrm{d}\mathbf{F} = h \left\{ F_c - \mathbf{F} : \frac{\mathrm{d}\varepsilon_q^p}{\|\mathrm{d}\varepsilon_q^p\|} \exp\left[m(M - \eta) + n\psi \right] \right\} \mathrm{d}\varepsilon_q^p \tag{16}$$

where $\psi = e - e_c$ is the state parameter defined by Been and Jefferies (1985), h, m and n are the model parameters, $F_c = \sqrt{\mathbf{F}_c : \mathbf{F}_c}$ is the critical value of normalization of the fabric tensor, $\mathrm{d}\varepsilon_q^p$ is the plastic deviatoric strain increment, M is the critical stress ratio, η is the stress ratio.

The localization of global variables to local variables (e.g. Eq. (13)) is accomplished through the use of the static hypothesis. However, the averaging of the local variables to the global variables (e.g. Eqs. (11) and (12)) requires the integration of the local variables over the contact orientations. Assume Ψ is a local variable, the integration of Ψ over the contact orientations can be discretized as the summation of the local variables weighted by the directional distribution function based on the Gauss integration method over the sphere (Bažant and Oh, 1986):

$$\langle \Psi \rangle = \int_{\Omega} \xi(\mathbf{n})\Psi(\mathbf{n})\mathrm{d}\Omega \approx \sum_{c=1}^{N} w(\mathbf{n})\xi(\mathbf{n})\Psi(\mathbf{n}) \tag{17}$$

where $w(\mathbf{n})$ is the weights of the Gauss integration points.

2.4. Global mixed load control

The global mixed load control is used to obtain the stress increment under general mixed stress and strain loadings. As mentioned by Zhao et al. (2018a), one of the difficulties in implementing a micromechanical model based on the static hypothesis is to calculate the stress increment under mixed stress and strain loadings. To overcome the difficulties, Zhao et al. (2018a) expressed the loading control as linearized constraints (Bardet and Choucair, 1991):

$$\mathbf{S}\mathrm{d}\boldsymbol{\sigma}^n + \mathbf{E}\mathrm{d}\boldsymbol{\varepsilon}^n = \mathrm{d}\mathbf{X}^n \tag{18}$$

where $\mathbf{S}$ and $\mathbf{E}$ are constraint matrices depending on the loading path which can be found in Zhao et al. (2018a) and $\mathrm{d}\mathbf{X}$ is the mixed stress and strain increments. The stress and strain increments can be obtained by combining the linearized constraints with the stress–strain relationship at the macroscopic level:

$$\mathrm{d}\boldsymbol{\sigma}^n = \mathbf{D}^{ep}\mathrm{d}\boldsymbol{\varepsilon}^n \tag{19}$$

where $\mathbf{D}^{ep}$ is the elastoplastic stiffness matrix.

The challenge in solving Eqs. (18) and (19) lies in the unavailability of the elastoplastic stiffness $\mathbf{D}^{ep}$. Zhao et al. (2018a) developed an iterative algorithm to solve the mixed stress and strain increment problem. Initially, the stress and strain increments are predicted using the elastic stiffness matrix $\mathbf{D}^e$. Subsequently, these predicted values are corrected to adhere to the plasticity of the local contact behaviors. Detailed information can be found in Zhao et al. (2018a).

2.5. Implementation of the CHY model

Fig. 1 shows the implementation of the CHY model based on the above sections.

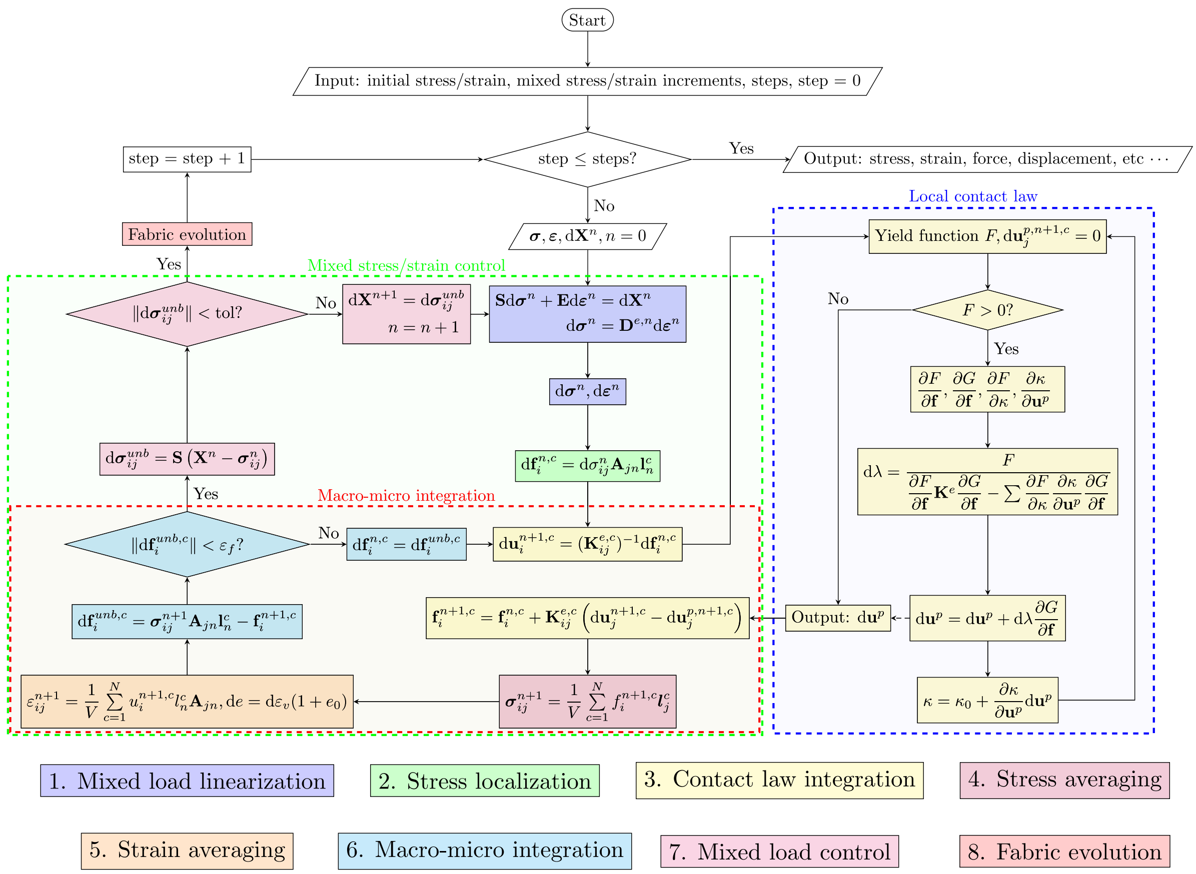

Fig. 1. Implementation of the CHY model.

3. Critical-state compatible CHY micromechanical model

Although Chang and Hicher (2005) and Zhao and Kruyt (2020) described that the CHY model satisfies the critical state theory, no theoretical proof was provided. In this section, we propose a modified CHY model that is compatible with the critical state theory with a theoretical proof.

3.1. Modifications for critical-state compatibility

As shown in Fig. 1, the local contact force is derived from the global stress using the static hypothesis presented in Eq. (13). The contact displacement is then calculated based on an elastic trial employing the elastic stiffness matrix, resulting in a fully elastic contact displacement with no plastic deformation. Since the strain is derived from the contact displacement according to Eq. (11), it also remains entirely elastic. Conversely, the contact force is updated according to the elastoplastic contact law, and the stress is calculated using the Love–Weber formula in Eq. (12). Thus, it can be concluded that the stress consists of both elastic and plastic components, whereas the strain is purely elastic.

To ensure that the plastic deformation is correctly accounted in the strain, the contact displacement is added by the plastic displacement generated by the elastoplastic contact law:

$$\left(\mathrm{d}\mathbf{u}_i^c\right)' = \mathrm{d}\mathbf{u}_i^{e,c} + \mathrm{d}\mathbf{u}_i^{p,c} = \mathrm{d}\mathbf{u}_i^{e,c} + \mathrm{d}\lambda_i \begin{bmatrix} D_i^c & n_{si}^c & n_{ti}^c \end{bmatrix}^{\mathsf{T}} \tag{20}$$

where $\mathrm{d}\mathbf{u}_i^{e,c}$ is the elastic displacement, $\mathrm{d}\mathbf{u}_i^{p,c}$ is the plastic displacement, $\mathrm{d}\lambda_i$ is the plastic multiplier, and n_{si}^c and n_{ti}^c are the shear direction vectors. The volumetric strain can be calculated from Eq. (11):

$$\begin{aligned} \mathrm{d}\varepsilon_v &= \mathrm{tr}\left(\mathrm{d}\varepsilon_{ij}\right) = \mathrm{tr}\left[\frac{1}{V}\sum_{c=1}^{N} \mathrm{d}\mathbf{u}_i^c \mathbf{l}_n^c \mathbf{A}_{jn}^{\mathrm{iso}} \left(\mathbf{A}_{jn}^{\mathrm{iso}}\right)^{-1} \mathbf{A}_{jn}\right] \\ &= \mathrm{tr}\left[\mathrm{d}\varepsilon_{ij}^{\mathrm{iso}} \left(\mathbf{A}_{jn}^{\mathrm{iso}}\right)^{-1} \mathbf{A}_{jn}\right] \end{aligned} \tag{21}$$

where $\mathrm{d}\varepsilon_{ij}^{\mathrm{iso}}$ is the strain increment when no fabric anisotropy is considered and its diagonal components can be calculated as:

$$\begin{aligned} \mathrm{d}\varepsilon_{11}^{\mathrm{iso}} &= \frac{1}{2rN}\sum_{c=1}^{N}\left(\mathrm{d}u_n \cos^2\gamma - \mathrm{d}u_s \sin\gamma\cos\gamma\right) \\ \mathrm{d}\varepsilon_{22}^{\mathrm{iso}} &= \frac{1}{2rN}\sum_{c=1}^{N}\left(\mathrm{d}u_n \sin^2\gamma\cos^2\beta + \mathrm{d}u_s \sin\gamma\cos\gamma\cos^2\beta - \mathrm{d}u_t \sin\gamma\sin\beta\cos\beta\right) \\ \mathrm{d}\varepsilon_{33}^{\mathrm{iso}} &= \frac{1}{2rN}\sum_{c=1}^{N}\left(\mathrm{d}u_n \sin^2\gamma\sin^2\beta + \mathrm{d}u_s \sin\gamma\cos\gamma\sin^2\beta + \mathrm{d}u_t \sin\gamma\sin\beta\cos\beta\right) \end{aligned} \tag{22}$$

The volumetric strain for isotropic materials can be calculated as:

$$\mathrm{d}\varepsilon_v^{\mathrm{iso}} = \mathrm{tr}\left(\mathrm{d}\varepsilon_{ij}^{\mathrm{iso}}\right) = \frac{1}{2rN}\sum_{c=1}^{N}\mathrm{d}u_n \tag{23}$$

Eq. (23) indicates that the macroscopic volumetric strain is determined entirely by the contact normal displacement for isotropic materials. This is desirable because it fulfills the requirement that zero contact normal displacement leads to zero volumetric strain which means that the microscopic force–dilatancy relationship aligns with

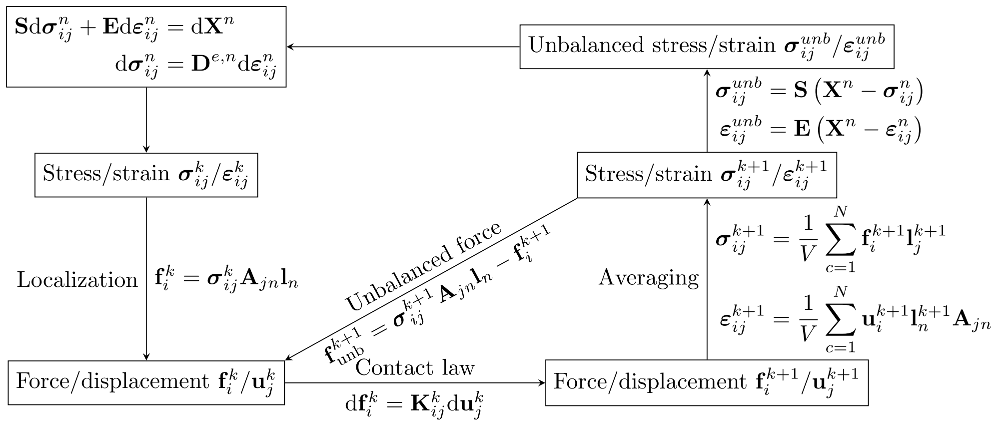

Fig. 2. Implementation of the modified model.

the macroscopic stress–dilatancy relationship. However, for the case of anisotropic materials, this requirement is not satisfied because of the fabric tensor $\mathbf{A}_{jn}$.

For the CHY model, considering that the critical state is introduced in the contact law to achieve the critical state in the macro scale, it is reasonable to assume that the critical state at the micro-scale and macro-scale should be consistent. For isotropic materials, previous studies (Chang et al., 2009; Yin and Chang, 2009; Yin et al., 2014; Hicher and Chang, 2007; Zhao et al., 2017) have shown that the CHY model achieves the critical state at the macro-scale because the microscopic force–dilatancy relationship is automatically consistent with the macroscopic stress–dilatancy relationship. However, for anisotropic materials, they are not necessarily consistent. Therefore, To ensure that the critical state at the micro-scale and macro-scale are consistent, the fabric tensor $\mathbf{A}_{jn}$ is ignored in the calculation of the volumetric strain. That is to say, Eq. (21) is modified as:

$$\mathrm{d}\varepsilon'_{ij} = \frac{1}{V}\sum_{c=1}^{N}\left(\mathrm{d}\mathbf{u}^c_i\right)'\mathbf{l}^c_n\mathbf{A}^{\mathrm{iso}}_{jn} \tag{24}$$

Both Eqs. (20) and (24) result in the micromechanical model violating the principle of energy conservation, as follows:

$$\boldsymbol{\sigma}_{ij}\mathrm{d}\boldsymbol{\varepsilon}_{ij} = \frac{1}{V}\sum_{c=1}^{N}\mathbf{f}^c_i\mathrm{d}\mathbf{u}^c_i \tag{25}$$

When the applied strain is localized to contact displacement, the contact displacement is added by the plastic displacement, and the average strain tensor is adjusted to exclude the fabric tensor. This adjustment results in an imbalance between the macroscopic strain and the microscopic contact displacement. To resolve this issue, both stress and strain are evaluated to ensure equilibrium between contact forces and displacements. In the mixed-load control algorithm, the unbalanced stress and strain are determined as follows:

$$\begin{aligned}\boldsymbol{\sigma}^{unb}_{ij} &= \mathbf{S}\left(\mathbf{X}^n - \boldsymbol{\sigma}^n_{ij}\right)\\ \boldsymbol{\varepsilon}^{unb}_{ij} &= \mathbf{E}\left(\mathbf{X}^n - \boldsymbol{\varepsilon}^n_{ij}\right)\end{aligned} \tag{26}$$

where $\mathbf{X}^n = \mathbf{X}^{n-1} + \mathrm{d}\mathbf{X}^n$ is the mixed load vector. Then, the unbalanced stress and strain will be checked:

$$\left\|\frac{\mathbf{S}\boldsymbol{\sigma}^{unb}_{ij}}{\left\|\boldsymbol{\sigma}_{ij}\right\|} + \frac{\mathbf{E}\boldsymbol{\varepsilon}^{unb}_{ij}}{\left\|\boldsymbol{\varepsilon}_{ij}\right\|}\right\| \le \mathrm{tol} \tag{27}$$

If the relative error exceeds the specified tolerance, tol, the unbalanced stress and strain are passed to the subsequent step:

$$\mathrm{d}\mathbf{X}^{n+1} = \mathbf{S}\boldsymbol{\sigma}^{unb}_{ij} + \mathbf{E}\boldsymbol{\varepsilon}^{unb}_{ij} \tag{28}$$

Fig. 2 shows the implementation of the modified model. The only difference between the modified model and the original model is the balancing of strain $\boldsymbol{\varepsilon}^{unb}_{ij}$. For the original model, the energy conservation principle is automatically satisfied when the macroscopic stress and contact forces are balanced according to Eq. (13). This means $\boldsymbol{\varepsilon}^{unb}_{ij} = 0$ satisfies automatically.

For the modified model, $\boldsymbol{\varepsilon}^{unb}_{ij} \neq 0$ because of the consideration of plastic displacement and modification of the averaging strain tensor. In this case, the unbalanced strain can be rewritten as:

$$\boldsymbol{\varepsilon}^{unb}_{ij} = \mathrm{d}\varepsilon_{ij} - \mathrm{d}\varepsilon'_{ij} = \frac{1}{V}\sum_{c=1}^{N}\mathrm{d}\mathbf{u}^c_i\mathbf{l}^c_n\mathbf{A}_{jn} - \frac{1}{V}\sum_{c=1}^{N}\left(\mathrm{d}\mathbf{u}^c_i\right)'\mathbf{l}^c_n\mathbf{A}^{\mathrm{iso}}_{jn} \tag{29}$$

The unbalanced strain is then passed to the mixed-load control algorithm, where it is converted to stress increments with the stiffness matrix $\mathbf{D}$. The stress increments are then localized to the contact forces based on the static hypothesis in the next iteration. Finally, the mixed-load control algorithm is iterated until the unbalanced strain $\boldsymbol{\varepsilon}^{unb}_{ij}$ converges to zero. This iteration is very much like the plastic correction algorithm in conventional elastoplastic models where the plastic strain is eventually generated and the stress is updated to correct the elastic trial stress. Following the iterative process, Eq. (29) demonstrates that despite modifications to contact displacements and adjustments to the averaging strain tensor, the strain remains equivalence to its pre-modification value. Consequently, the energy conservation principle remains satisfied.

3.2. Proof of the critical state compatibility

With the above modifications, the void ratio converges to the critical state line, as the condition described by Eq. (23) ensures that macroscopic strain reaches the critical state when microscopic displacement also reaches the critical state. For dense sand, $e < e_c$, the dilatancy D^c_i is negative near the critical state, resulting in a negative plastic normal displacement and therefore negative volumetric strain is generated according to Eq. (24). According to Eq. (9), the void ratio increases with the negative volumetric strain, and eventually, the void ratio approaches the critical void ratio e_c.

The uniqueness of the stress ratio at the critical state still requires a theoretical proof. Under conventional triaxial loading condition, the mean and deviatoric stresses can be simplified as the following equations based on Eq. (12):

$$\begin{aligned}p &= \frac{1}{3}\mathrm{tr}\left(\boldsymbol{\sigma}\right) = \frac{2r}{3V}\sum_{c=1}^{N}f_n\\ q &= \sqrt{3J_2} = \frac{1}{2}\left|2\sigma_1 - \left(\sigma_2+\sigma_3\right)\right|\\ &= \frac{r}{V}\sum_{c=1}^{N}\left|2f_n - 3\left(f_n\sin^2\gamma + f_s\sin\gamma\cos\gamma\right)\right|\end{aligned} \tag{30}$$

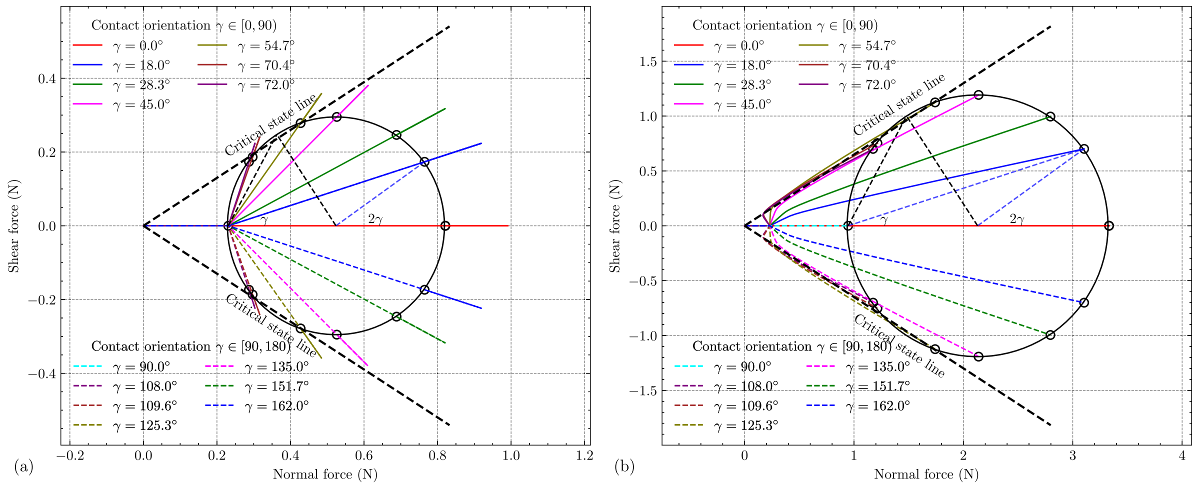

Fig. 3. Evolution of contact forces: (a) drained triaxial test; (b) undrained triaxial test.

where σ_1, σ_2, and σ_3 are the principal stresses, p is the mean stress, q is the deviatoric stress, J_2 is the second invariant of the deviatoric stress tensor. Based on the static hypothesis shown in Eq. (13), the contact normal and shear forces can be calculated as:

$$
\begin{aligned}
f_n &= \frac{3V}{2rN}\left(\sigma_1 \cos^2\gamma + \sigma_3 \sin^2\gamma\right) = f_{n13} + R_{13}\cos 2\gamma \\
f_s &= \frac{3V}{2rN}\left(\sigma_1 \sin\gamma\cos\gamma - \sigma_3 \sin\gamma\cos\gamma\right) = R_{13}\sin 2\gamma, f_t = 0 \\
f_{n13} &= \frac{3V}{4rN}\left(\sigma_1 + \sigma_3\right), R_{13} = \frac{3V}{4rN}\left(\sigma_1 - \sigma_3\right)
\end{aligned}
\tag{31}
$$

It is noteworthy that the normal and shear forces in Eq. (31) lie on a circle with the center at $(f_{n13}, 0)$ and a radius of R_{13}. For further demonstration, drained and undrained triaxial tests are simulated using the original model with the parameters in Zhao et al. (2018a), and the evolution of the contact forces under drained and undrained conditions is presented in Fig. 3. As shown in the figure, under drained and undrained conditions, the contact normal and shear forces lie on a microscopic Mohr's circle.

Substituting Eq. (31) into Eq. (30) and performing integrations over all contact directions, the stress ratio η can be expressed as:

$$
p = \frac{2rN}{3V}\left(f_{n13} - \frac{R_{13}}{3}\right), q = \frac{rN}{V}\frac{4|R_{13}|}{3}, \eta = \frac{q}{p} = \frac{6|R_{13}|}{3f_{n13} - R_{13}} \tag{32}
$$

According to Fig. 3, $R_{13} = \pm f_{n13}\sin\phi$ at critical state (positive for triaxial compression). Therefore, the stress ratio at critical state can be calculated as:

$$
M = \frac{6f_{n13}\sin\phi}{3f_{n13} \mp f_{n13}\sin\phi} = \frac{6\sin\phi}{3 \mp \sin\phi} \tag{33}
$$

Eq. (33) shows that the stress ratio at critical state is unique and only depends on the friction angle ϕ. It is noteworthy that the stress ratio at critical state is same as the one in the Mohr–Coulomb model. Under general loading conditions, the critical stress ratio only depends on the friction angle ϕ and the intermediate stress ratio b. However, the derivation is complicated and will not be presented here.

The above analysis shows that the void ratio and stress ratio at critical state are unique in triaxial space, proving that the modified model is compatible with the critical state theory.

3.3. Summary of model parameters

Table 1 shows the summary of model parameters. The elasticity parameters for the contact law are related to the elastic moduli as shown in Eq. (3). The critical state and dilatancy parameters are similar to those in conventional macroscopic models. The parameter k_{pR} controls the shape of the yield surface and parameters h, m and n control the evolution of the fabric tensor.

Table 1
Summary of model parameters.

Category	Parameter	Description
Elasticity	k_{n0}	Initial normal stiffness
	n_e	Exponent of normal stiffness for normal force
	k_{rR}	Shear stiffness ratio
Yield surface	k_{pR}	A constant in yield surface
Critical state	ϕ_c	Critical friction angle
	e_{ref}	Reference critical void ratio
	λ	Slope of critical state line
	n_p	Exponent for effect of interlocking
Dilatancy	n_d	Exponent for effect of dilatancy
	A_d	A dilatancy parameter
Fabric evolution	F_{c0}	Norm of critical fabric tensor
	h	Constant to control velocity of fabric evolution
	m, n	Constants for effects of η and ψ on fabric evolution

4. Evaluations of the modified model

To evaluate the modified model at both macroscopical and microscopical scales, drained and undrained triaxial experiments and DEM simulations were collected from the literature. Table 2 summarizes the experiments used for model evaluations.

4.1. Calibration of model parameters

The model parameters for Hostun sand are mainly adopted from Zhao et al. (2018a) with minor modifications because of the consideration of plastic displacements. For the Toyoura sand, the calibrations of friction angle ϕ_c and critical state line parameters e_{ref} and λ are shown in Fig. 4.

According to Eq. (33), the friction angle should be around 20.3 degrees to match the critical stress ratio. However, because of the consideration of fabric anisotropy, the critical stress ratio for the micromechanical model is higher than the one in the isotropic case because there are more contacts in the loading direction to resist the loading. Therefore, the friction angle is recalibrated to 15.6 degrees to match the critical stress ratio. The parameters k_{n0} and k_{rR} can be calibrated from the value of Young's modulus and Poisson's ratio based on the relationship between contact stiffness and elastic moduli as shown in Eq. (3). Other parameters like k_{pR}, n_p, n_d, A_d and parameters for fabric evolution are difficult to be directly calibrated from the experimental data because they describe the microscopic interparticle behaviors which are not directly observable in the macroscopic experiments, despite the fact that they are indirectly related to the macroscopic behaviors. Therefore, these parameters are derived from

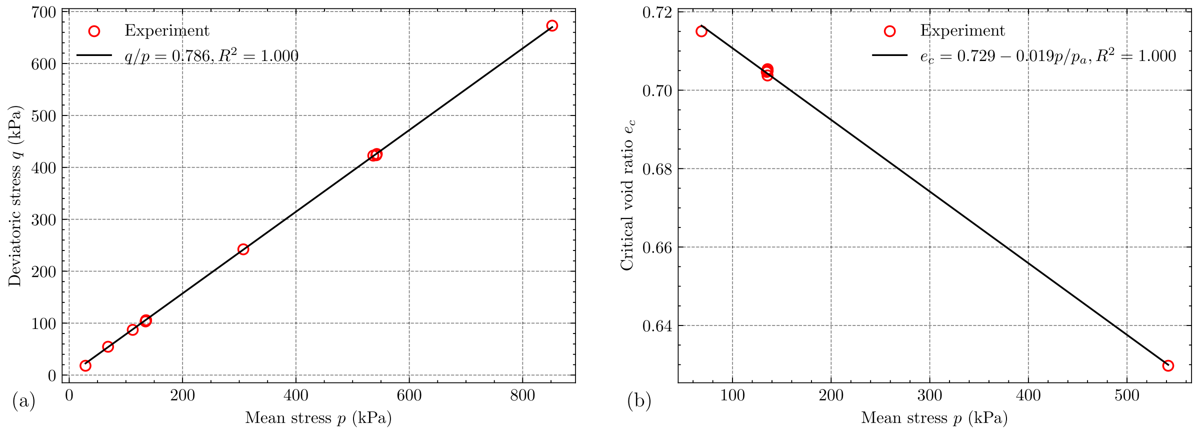

Fig. 4. Calibration of model parameters: (a) friction angle; (b) critical state line.

Table 2
Summary of experiments for model evaluations.

Sand	d_{50} (mm)	p_0 (kPa)	Drainage	e_0	Reference
Hostun	1.3	100/300/800	Drained	0.502–0.722	Biarez and Hicher (1994)
Toyoura	0.22	50/100/400	Drained/Undrained	0.572–0.713	Gu et al. (2014)

Table 3
Calibrated parameters for experiments by Biarez and Hicher (1994) and Gu et al. (2014).

Sand	k_{n0} (N/mm)	n_e	k_{rR}	k_{pR}	ϕ_c (°)	e_{ref}	λ	ξ	n_p	n_d	A_d	F_{c0}	h	m	n
Hostun	30.2	1.06	0.65	0.11	31.9	0.80	0.05	1.00	1.59	2.38	0.73	–	–	–	–
Toyoura	68.7	0.39	0.23	0.25	15.6	0.733	0.019	1.00	1.84	5.02	1.50	0.41	453	2.06	0.01

previous studies (Chang and Hicher, 2005; Zhao et al., 2018a; Zhao and Kruyt, 2020) with minor modifications to match the experimental results based on an optimization algorithm. The calibrated parameters are listed in Table 3.

4.2. Drained triaxial experiments on Hostun sand

Fig. 5 presents comparisons between simulations and triaxial experiments on Hostun sand. The results indicate that the modified model accurately captures the stress–strain behavior of Hostun sand under various confining pressures and densities. At the critical state, both deviatoric stress and void ratio converge to the critical state values. The evolution of local contact forces on Hostun sand is illustrated in Fig. 6. The relationship between normal and shear forces appears linear, comparable to the relationship between the mean and deviatoric stresses observed in drained triaxial experiments. This is attributed to the static hypothesis in Eq. (13), which assumes uniform stress distribution at the microscopic level within the heterogeneous material.

For the relationship between the shear force and shear displacement in Fig. 6, we can conclude that the shear forces are mobilized to different degrees at different directions. The active contact forces are mainly concentrated in directions from 45° to 72°. The largest shear displacement is observed at 55° which is very close to the direction $45° + \phi/2$, showing that a shear band is most likely to form in this direction. The relationship between the shear force and shear displacement is very much like the stress–strain relationship in the macroscopic scale, where a peak force is observed for dense sand and the peak force ratio decreases with the increase of the normal force.

The distribution of normal and shear displacements in various directions is shown in Fig. 7. Notably, the largest normal and shear displacements occur at the orientation angle of 55°, as previously discussed. In experiments with dense sand, dilative responses are observed within the shear band, while experiments with loose sand show contractive responses. This aligns with the macroscopic stress–strain relationship, where dense sand exhibits a dilative response and loose sand shows a contractive response. Consequently, the averaging strain tensor in Eq. (24) effectively links microscopic and macroscopic dilatancy behaviors. Furthermore, the shear displacement at an orientation angle of 55° increases rapidly, suggesting a shear band is likely to form in this direction.

4.3. Drained and undrained triaxial DEM simulations

4.3.1. Macroscopic behaviors

Fig. 8 shows comparison between model predictions and DEM simulations conducted by Gu et al. (2014) for drained triaxial experiments. In general, the results indicate that the simulations align well with the experimental data. A softening behavior is observed in dense sand, whereas loose sand exhibits a continuous hardening behavior. Notably, all experiments show contraction in the initial stage; subsequently, dense sand undergoes dilation, while loose sand continues to contract. Both the stress ratio and void ratio converge to the critical state values.

For experiments with same density and different confining pressures, the results show that, despite having the same density, the sample exhibits a more pronounced dilative response at lower confining pressure (50 kPa) compared to higher confining pressure (400 kPa), aligning with observations from previous studies (Alonso-Marroquín et al., 2006). In the 400 kPa experiment, the simulation underestimates the softening behavior, likely because the model overestimates the impact of confining pressure on the dilative response in the critical state line. However, the model successfully captures the critical state behaviors, as both the stress ratio and void ratio converge to the critical state values.

Fig. 9 shows comparisons between model predictions and DEM simulations conducted by Gu et al. (2014) for undrained triaxial experiments. In general, the simulations align well with the experimental data. However, for very dense sand ($e_0 = 0.572$), the simulation overestimates the dilative response compared to the DEM results. In

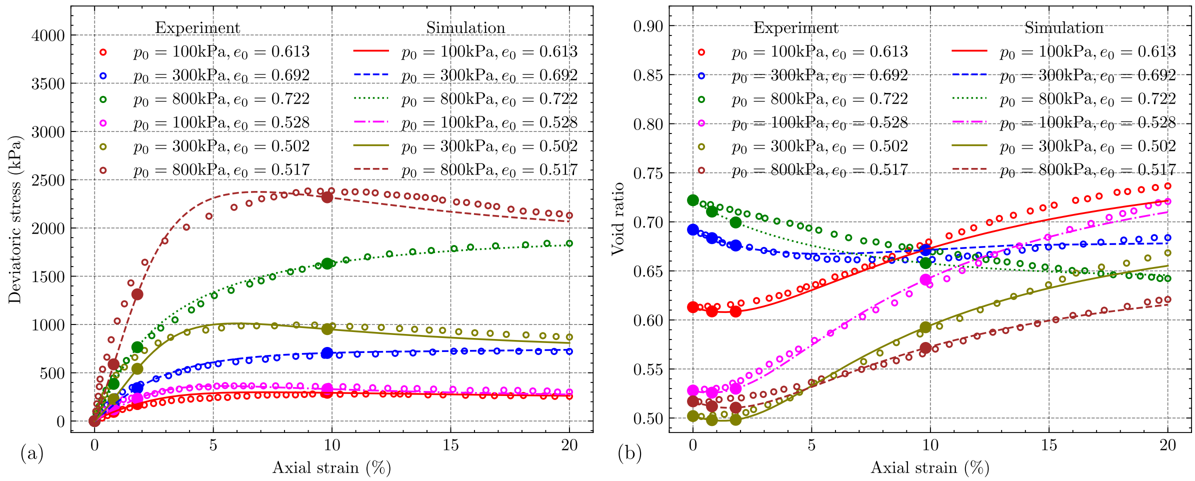

Fig. 5. Comparison between the simulations and experiments on Hostun sand: (a) deviatoric stress; (b) void ratio.

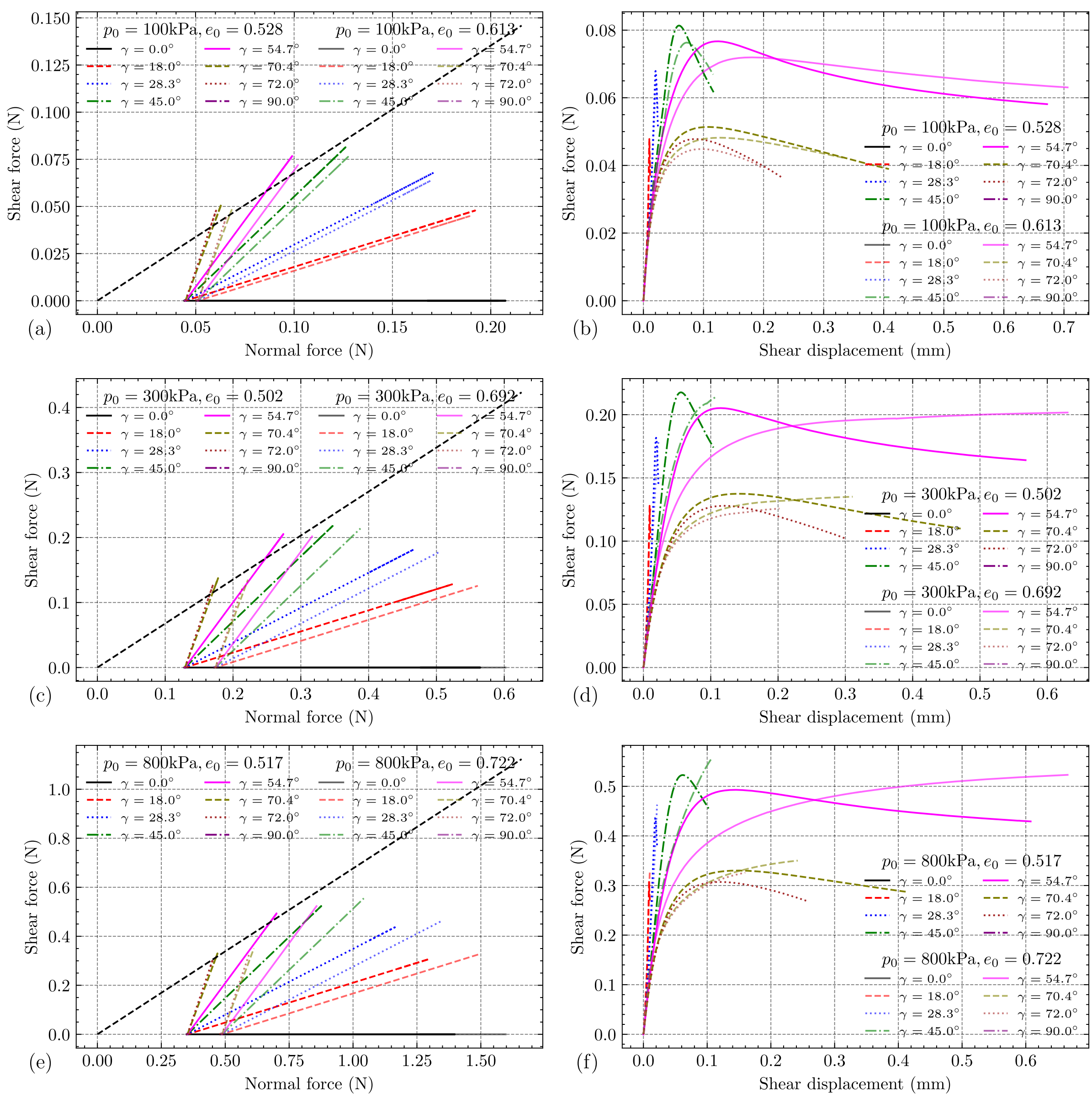

Fig. 6. Evolution of loc forces on Hostun sand: (a)(c)(e) normal force vs. shear force for different densities and confining pressures; (b)(d)(f) shear displacement vs. shear force for different densities and confining pressures.

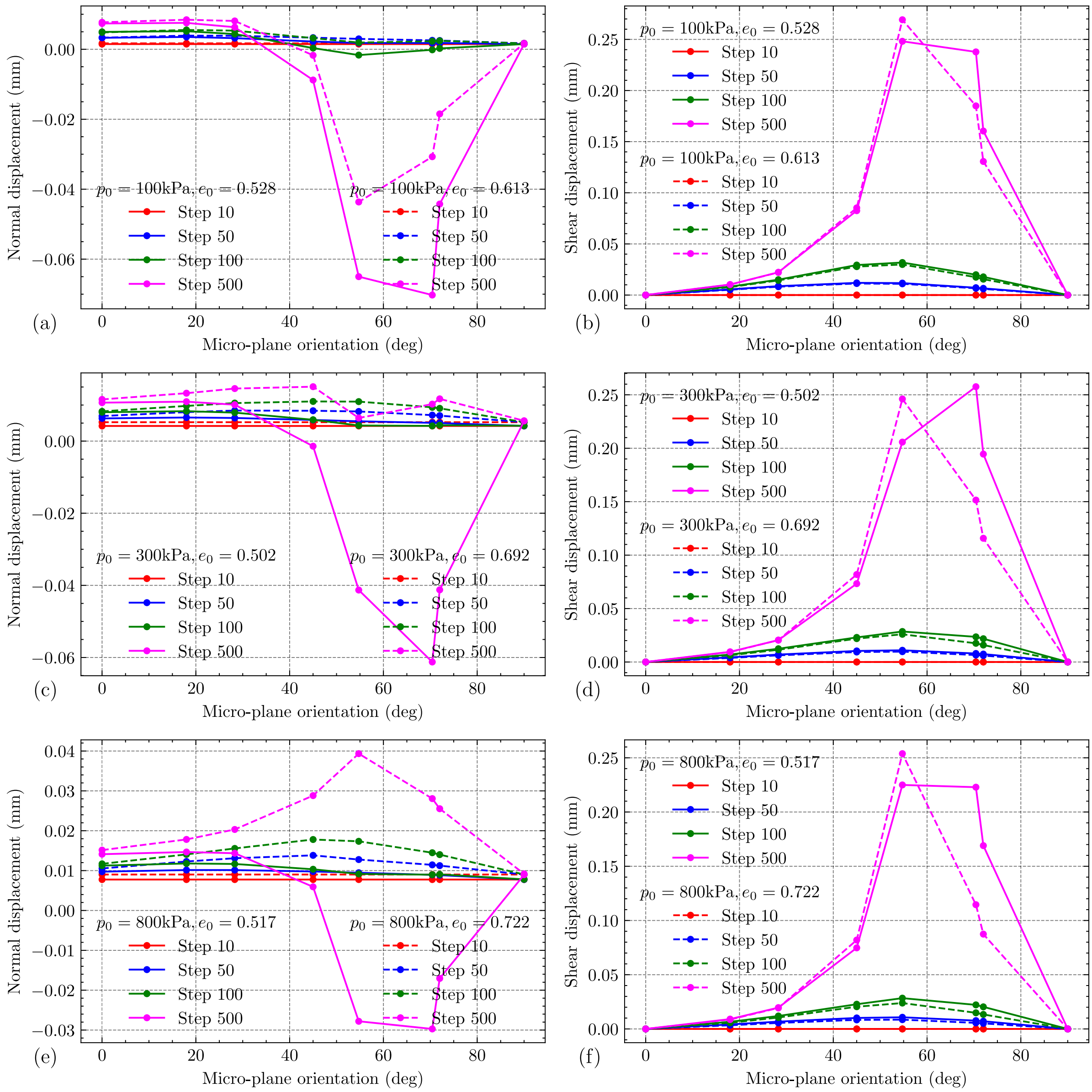

Fig. 7. Distribution of normal and shear displacements in different directions: (a)(c)(e) normal displacement for different densities and confining pressures; (b)(d)(f) shear displacement for different densities and confining pressures.

the case of very loose sand $e_0 = 0.713$, the DEM results exhibit static liquefaction, whereas the simulation predicts a steady state, indicating that the simulation underestimates the contractive response. For other experiments, the simulation results agree closely with the DEM results. These findings suggest that the model underestimates the contractive response for very loose sand. This discrepancy highlights that the contact dilatancy model in Eq. (7) overestimates the dilatancy behavior of soils. Further investigation is necessary to improve the model; however, this is beyond the scope of this paper.

For experiments with same density and different confining pressures, the results show that the sample exhibits a more pronounced dilative response at lower confining pressure (50 kPa) compared to higher confining pressure (400 kPa) which is similar with the drained triaxial experiments. Both the stress ratio and void ratio converge to the critical state values.

In summary, the modified model accurately aligns with the experimental data from both drained and undrained triaxial experiments. Both the stress ratio and void ratio converge to their respective critical state values. Additionally, it successfully simulates the observed dilative and contractive responses, although minor discrepancies remain for extremely dense or loose sand conditions.

4.3.2. Fabric anisotropy

Chantawarangul (1993) derived that the stress ratio can be expressed in terms of fabric anisotropies based on the Love–Weber formula:

$$\frac{q}{p} = 0.4\alpha_r + 0.4\alpha_n + 0.6\alpha_t \tag{34}$$

where α_r, α_n, and α_t are the fabric anisotropies of the contact normal, normal and shear forces, respectively. The fabric anisotropies can be calculated as:

$$\alpha_r = \sqrt{\frac{3}{2}\mathbf{F}^r_{ij} : \mathbf{F}^r_{ij}}, \alpha_n = \sqrt{\frac{3}{2}\mathbf{F}^n_{ij} : \mathbf{F}^n_{ij}}, \alpha_t = \sqrt{\frac{3}{2}\mathbf{F}^t_{ij} : \mathbf{F}^t_{ij}} \tag{35}$$

where $\mathbf{F}^r_{ij}$, $\mathbf{F}^n_{ij}$, and $\mathbf{F}^t_{ij}$ are the deviatoric parts of the corresponding fabric tensors. Detailed derivations can be found in literature (Chantawarangul, 1993; Ouadfel and Rothenburg, 2001).

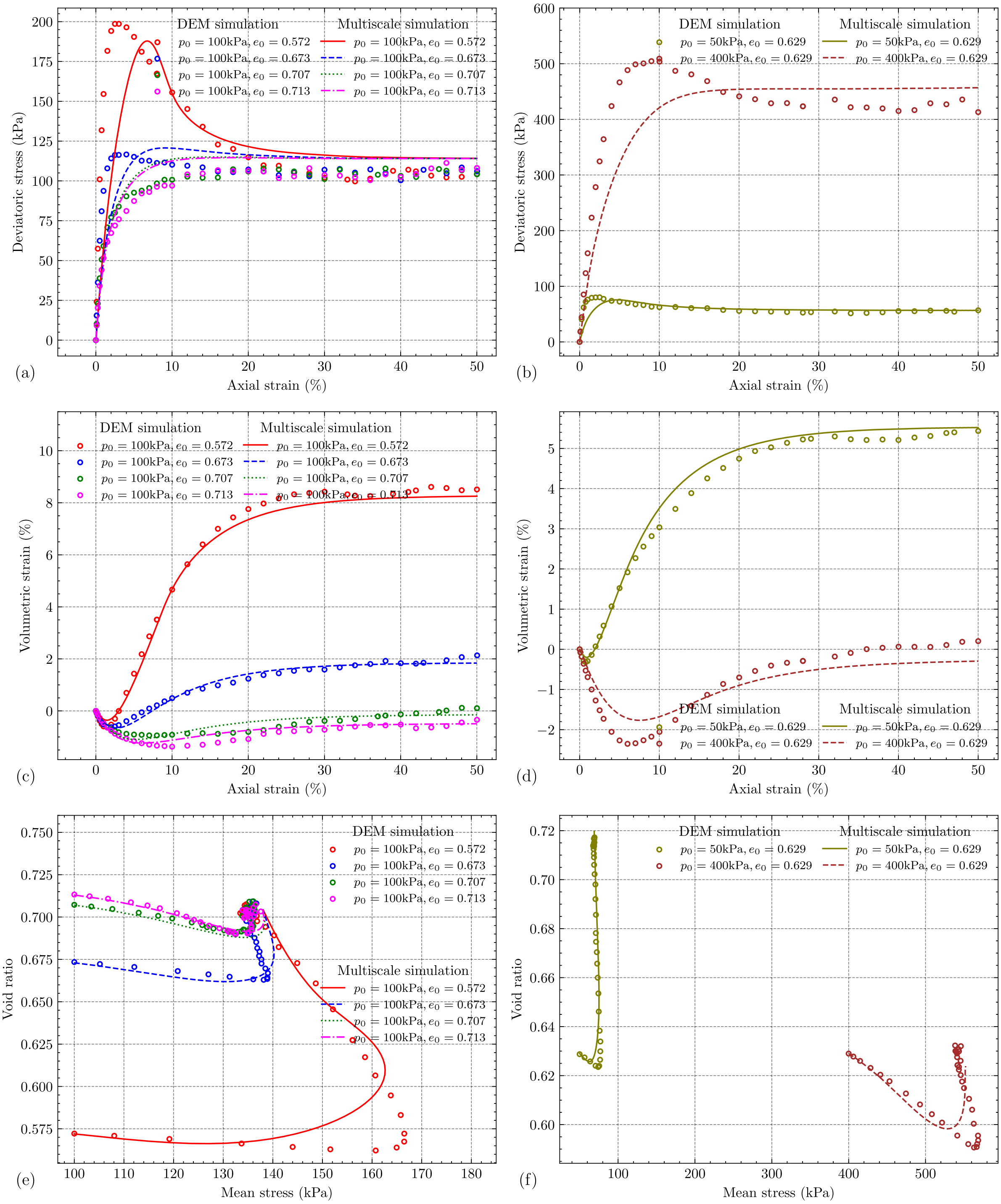

Fig. 8. Comparison between model predictions and DEM simulations by Gu et al. (2014): (a–b) deviatoric stress; (c–d) volumetric strain; (e–f) void ratio.

Fig. 10 presents a comparison of model predictions and DEM simulations from Gu et al. (2014), focusing on the fabric anisotropy of contact normals. The simulations demonstrate strong agreement with the experimental findings. Notably, a unique state of fabric anisotropy is observed in both drained and undrained experiments, confirming the compatibility of the fabric evolution law in Eq. (16) with the anisotropic critical state theory. It is important to highlight that, in the model, fabric anisotropy is directly incorporated through the fabric tensor of contact normals, without the need to modify the yield surface or force–dilatancy relationship as required by conventional models (Li and Dafalias, 2012; Gao et al., 2014).

Fig. 11 shows the validation of the stress–force–fabric relationship. The results show that the stress ratio agrees well with the fabric anisotropies of the contact normal, normal and shear forces.

4.3.3. Comparison with the original model

To demonstrate the improvements of the modified model, the original model is employed simulate the drained triaxial experiments conducted by Gu et al. (2014) with the same parameters listed in Table 3.

Fig. 12 illustrates the comparison between the original and modified models at critical state. The results indicate that the stress ratios for

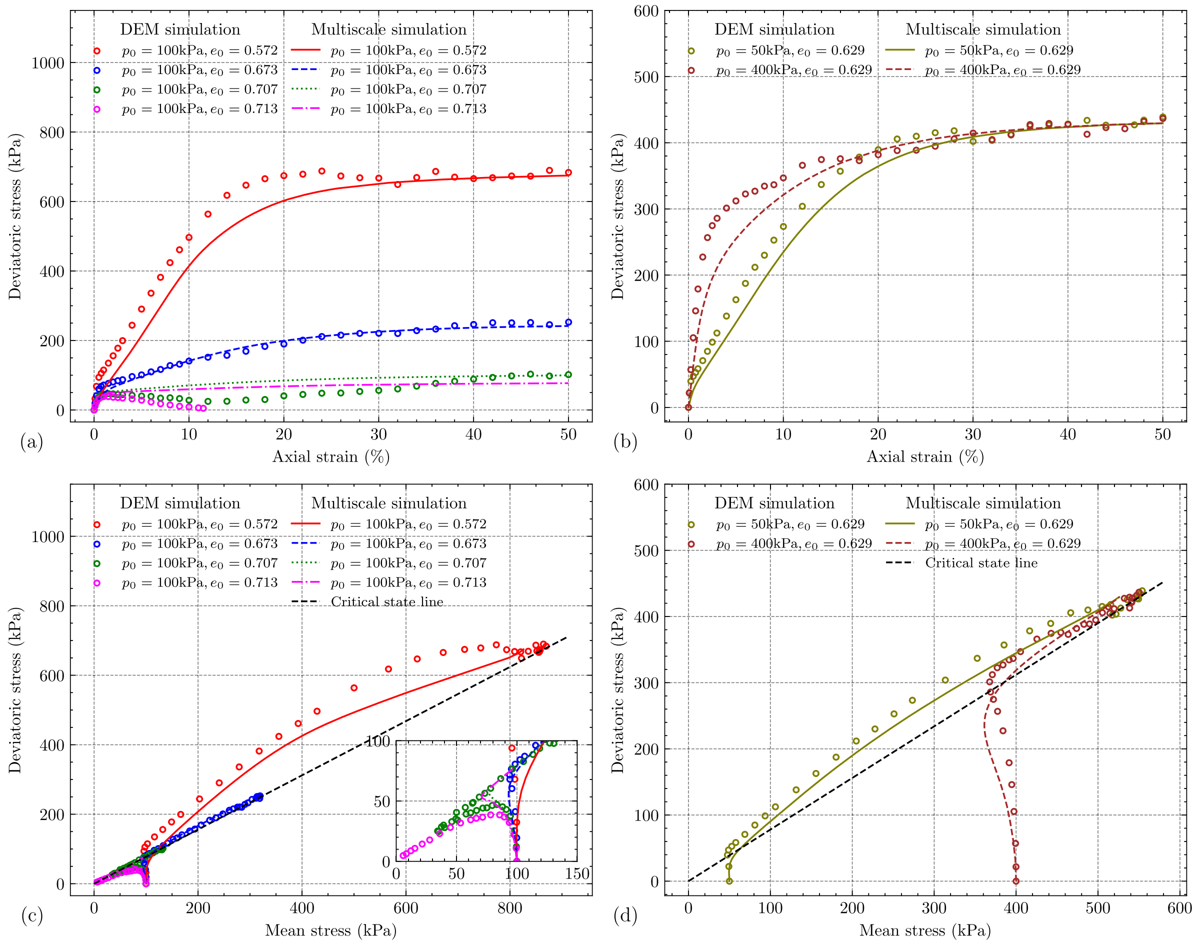

Fig. 9. Comparison between model predictions and DEM simulations by Gu et al. (2014): (a–b) axial strain vs. deviatoric stress; (c–d) mean stress vs. deviatoric stress.

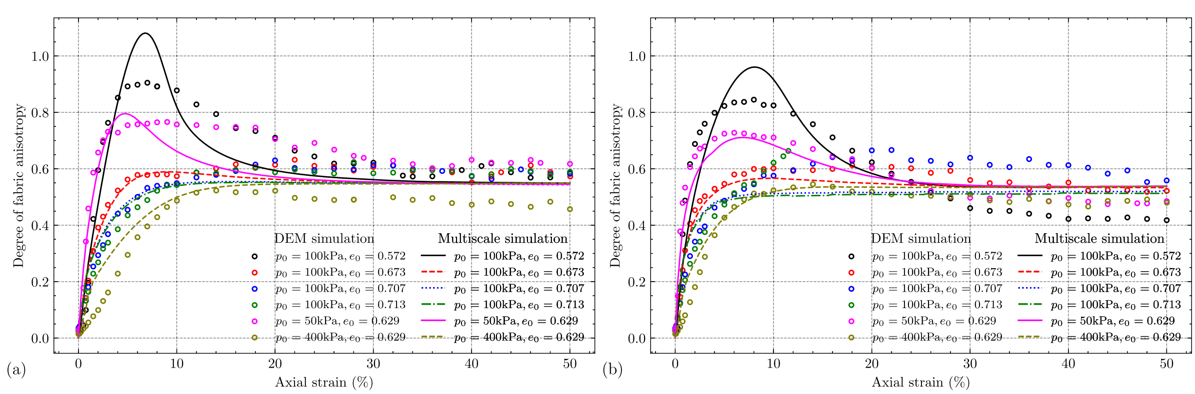

Fig. 10. Comparison between model predictions and DEM simulations by Gu et al. (2014) for fabric anisotropy: (a) drained experiments; (b) undrained experiments.

both original and modified models converge to the critical state value. This convergence can be attributed to the consideration of both elastic and plastic components in the contact force, which causes the stress ratio to stabilize at the critical state as the contact force reaches the critical state. However, the void ratio for the original model does not reach the critical state value, while the modified model does. This improvement is attributed to the modified strain formulation, which incorporates plastic deformation, effectively linking macroscopic strain with microscopic contact displacement, as described in Eqs. (20) and (24). Although the void ratio for the original model converges to a constant value under specific stress levels, it does not converge to the specified critical state line. Taking into account the fact that the original model does not account for plastic displacements, the strain is linearly related to the stress. This means that the convergence of the strain is in accordance with the contact forces, but not necessarily with the contact displacements. However, the introduction of the critical state line in the contact law originally by Chang and Hicher (2005) aims to capture the dilatancy and interlocking effects. For anisotropic materials, the microscopic force–dilatancy relationship is not consistent with the macroscopic stress–dilatancy relationship, leading to a discrepancy

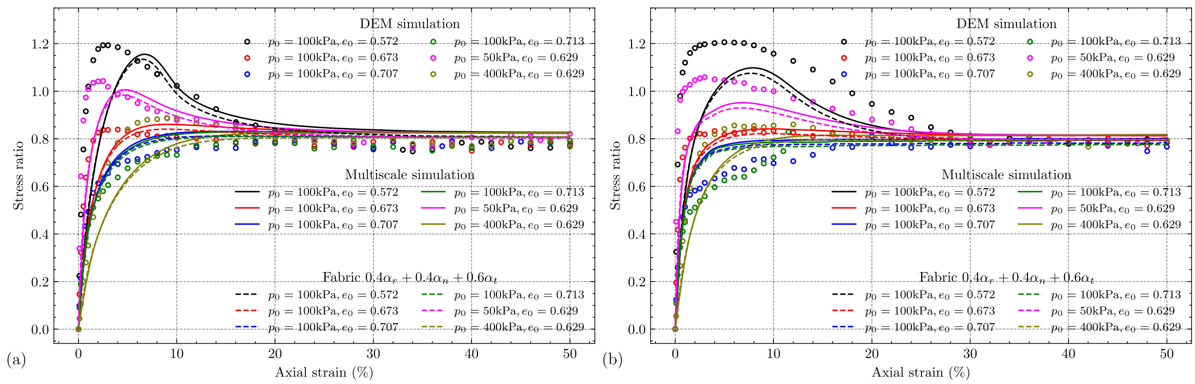

Fig. 11. Validation of stress–force–fabric relationship for DEM simulations by Gu et al. (2014): (a) drained experiments; (b) undrained experiments.

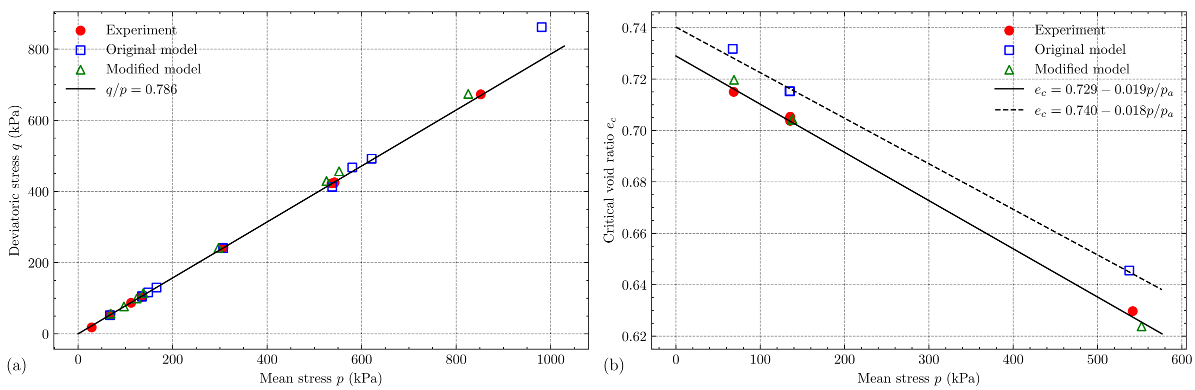

Fig. 12. Comparison between the original and modified models for critical state: (a) mean stress vs. deviatoric stress; (b) mean stress vs. void ratio.

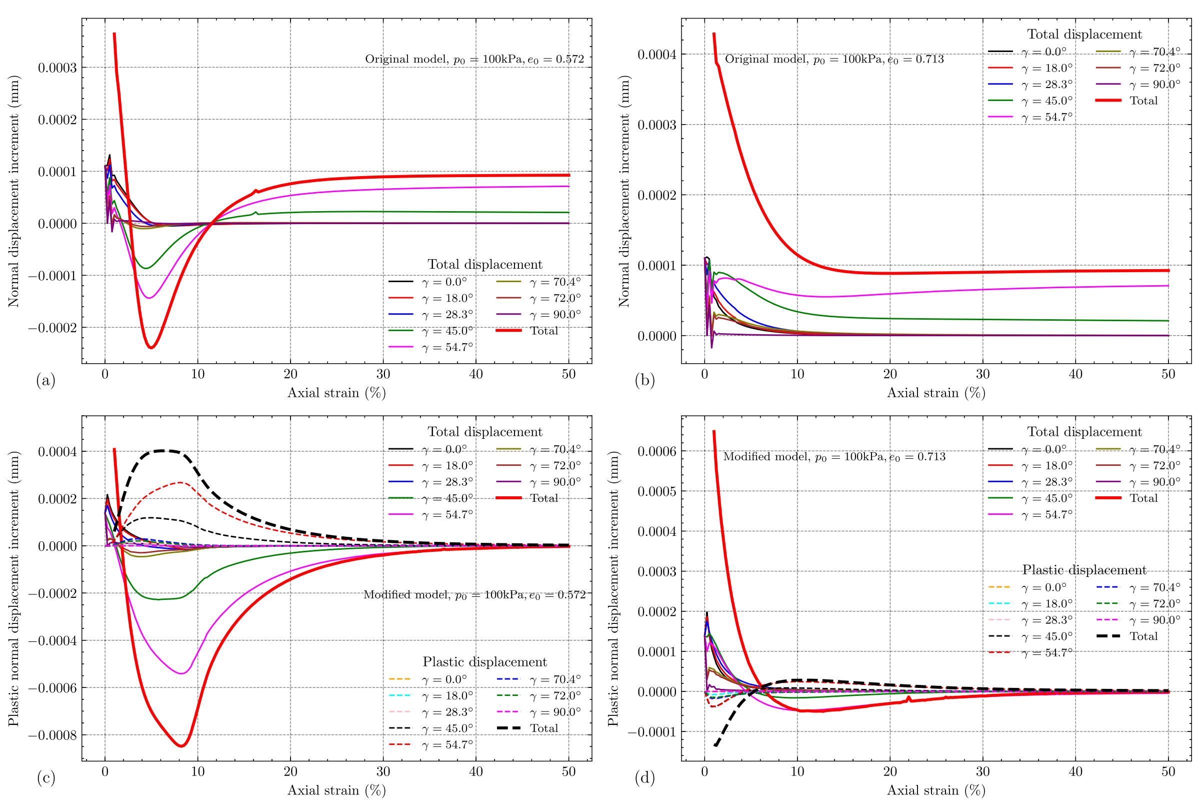

Fig. 13. Comparison between the original and modified models for contact normal displacement increment with drained experiments: (a) dense sand, original model; (b) loose sand, original model; (c) dense sand, modified model; (d) loose sand, modified model.

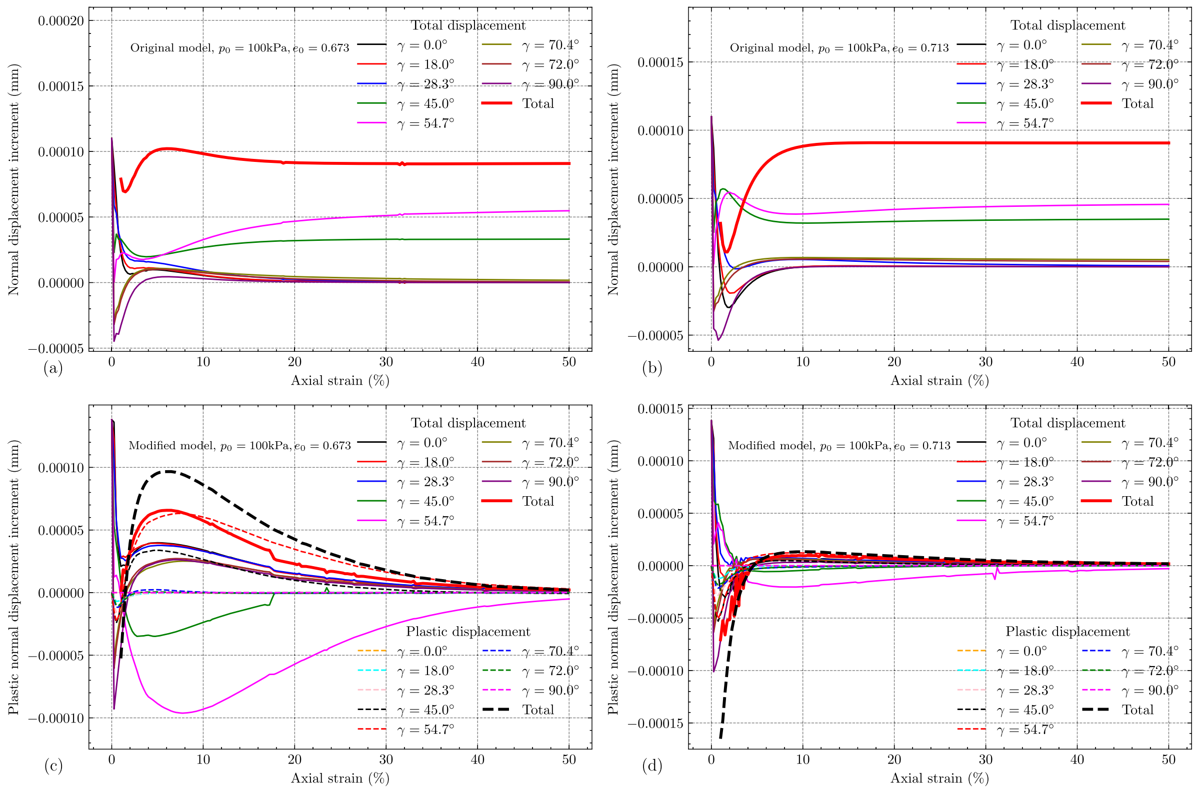

Fig. 14. Comparison between the original and modified models for contact normal displacement increment with undrained experiments: (a) dense sand, original model; (b) loose sand, original model; (c) dense sand, modified model; (d) loose sand, modified model.

between the void ratio and critical state line. The modification of the strain formulation in the modified model effectively resolves this issue, ensuring that the void ratio converges to the critical state line.

To demonstrate the fact that the strain in the modified model is governed by the contact displacement, the contact normal displacement increments for both dense sand and loose sand with drained experiments are compared between the original and modified models in Fig. 13. For the original model, the normal displacement increment at the orientation angles of 45° and 54.7° is not zero. However, the volumetric strain is zero at the critical state, which indicates that the local force–dilatancy relationship is not consistent with the macroscopic stress–dilatancy relationship. For the modified model, the total and plastic normal displacement increments at all orientation angles reach zero at the critical state, which indicates that the local force–dilatancy relationship is consistent with the macroscopic stress–dilatancy relationship.

For undrained experiments, similar comparisons are made between the original and modified models in Fig. 14. Although the macroscopic volumetric strain is controlled to be constant during loading, the microscopic normal displacement increment does not converge to zero at the critical state for the original model, especially for the orientation angles of 45° and 54.7°. Moreover, the total normal displacement increment converge to a constant value about 0.0001 mm whereas the macroscopic volumetric strain integrated from the normal displacement increment converges to zero, once again indicating that the local force–dilatancy relationship is not consistent with the macroscopic stress–dilatancy relationship. For the modified model, the total and plastic normal displacement increments at all orientation angles reach zero at the critical state, proving that the model aligns with the critical state theory at both the macroscopic and microscopic levels.

5. Conclusions

In this paper, a modified CHY model was proposed to ensure compatibility with the critical state theory. The model was validated using drained and undrained triaxial experiments and DEM simulations. Based on the results, the following conclusions can be drawn:

- The modified model aligns well with critical state theory, as both the stress ratio, void ratio, and fabric tensor converge to their respective critical state values. The model effectively captures the dilative and contractive responses observed in drained and undrained triaxial experiments.
- The stress–force–fabric relationship is well represented by the model, confirming its compatibility with the Love–Weber formula. The fabric anisotropy of contact normals is accurately captured by the model, demonstrating its consistency with the anisotropic critical state theory.
- The local contact behaviors are consistent with the macroscopic behaviors. The shear forces are mobilized to different degrees at different directions, and the shear displacement develops rapidly at the orientation angle of 55°, indicating that a shear band is likely to form in this direction.
- The modified model improves upon the original model by incorporating plastic displacement in total displacement which will be averaged to strain, ensuring that the void ratio converges to its critical state value. The model effectively links macroscopic strain with microscopic contact displacement, aligning

with critical state theory at both the macroscopic and microscopic levels.

Although the modified model demonstrates good compatibility with critical state theory, some discrepancies remain. For example, the model overestimates the dilative response for very dense sand and underestimates the contractive response for very loose sand. Further investigation is necessary to improve the model.

CRediT authorship contribution statement

Hai-Lin Wang: Writing – review & editing, Writing – original draft, Visualization, Validation, Investigation, Formal analysis. **Xiaoqiang Gu:** Writing – review & editing, Supervision, Methodology, Conceptualization. **Zhen-Yu Yin:** Writing – review & editing, Supervision, Conceptualization. **Chao-Fa Zhao:** Writing – review & editing, Methodology.

Declaration of Generative AI and AI-assisted technologies in the writing process

During the preparation of this work, the authors used ChatGPT in order to improve readability and language of the paper. After using this tool, the authors reviewed and edited the content as needed and take full responsibility for the content of the publication.

Declaration of competing interest

The authors declare that they have no known competing financial interests or personal relationships that could have appeared to influence the work reported in this paper.

Acknowledgments

The work presented in this paper is supported by National Natural Science Foundation of China (Grant No. 41772283 and 42361164615), the Fundamental Research Funds for the Central Universities, China and the Research Grants Council (RGC) of Hong Kong (Grant No. 15217220 and N_PolyU534/20). These supports are gratefully acknowledged.

Data availability

Data will be made available on request.

References

Alonso-Marroquín, F., Vardoulakis, I., Herrmann, H.J., Weatherley, D., Mora, P., 2006. Effect of rolling on dissipation in fault gouges. Phys. Rev. E 74 (3), 031306. http://dx.doi.org/10.1103/PhysRevE.74.031306.

Bardet, J.P., Choucair, W., 1991. A linearized integration technique for incremental constitutive equations. Int. J. Numer. Anal. Methods Geomech. 15 (1), 1–19. http://dx.doi.org/10.1002/nag.1610150102.

Bažant, P., Oh, B.H., 1986. Efficient numerical integration on the surface of a sphere. ZAMM - J. Appl. Math. Mech. / Z. Für Angew. Math. Und Mech. 66 (1), 37–49. http://dx.doi.org/10.1002/zamm.19860660108.

Been, K., Jefferies, M.G., 1985. A state parameter for sands. Géotech. 35 (2), 99–112. http://dx.doi.org/10.1680/geot.1985.35.2.99.

Biarez, J., Hicher, P.-Y., 1994. Elementary Mechanics of Soil Behaviour. AA Balkema.

Chang, C.S., Hicher, P.Y., 2005. An elasto-plastic model for granular materials with microstructural consideration. Int. J. Solids Struct. 42 (14), 4258–4277. http://dx.doi.org/10.1016/j.ijsolstr.2004.09.021.

Chang, C.S., Hicher, P.Y., Yin, Z.Y., Kong, L.R., 2009. Elastoplastic model for clay with microstructural consideration. J. Eng. Mech. 135 (9), 917–931. http://dx.doi.org/10.1061/(ASCE)EM.1943-7889.0000013.

Chang, C.S., Liao, C.L., 1994. Estimates of elastic modulus for media of randomly packed granules. Appl. Mech. Rev. 47 (1S), S197–S206. http://dx.doi.org/10.1115/1.3122814.

Chang, C.S., Yin, Z.-Y., 2010. Micromechanical modeling for inherent anisotropy in granular materials. J. Eng. Mech. 136 (7), 830–839. http://dx.doi.org/10.1061/(ASCE)EM.1943-7889.0000125.

Chang, C.S., Yin, Z.Y., Hicher, P.Y., 2011. Micromechanical analysis for interparticle and assembly instability of sand. J. Eng. Mech. 137 (3), 155–168. http://dx.doi.org/10.1061/(ASCE)EM.1943-7889.0000204.

Chantawarangul, K., 1993. Numerical Simulations of Three-Dimensional Granular Assemblies (Ph.D. thesis). University of Waterloo.

Cundall, P.A., Strack, O.D.L., 1979. A discrete numerical model for granular assemblies. Géotech. http://dx.doi.org/10.1680/geot.1979.29.1.47.

Darve, F., Nicot, F., 2005a. On flow rule in granular media: Phenomenological and multi-scale views (part II). Int. J. Numer. Anal. Methods Geomech. 29 (14), 1411–1432. http://dx.doi.org/10.1002/nag.467.

Darve, F., Nicot, F., 2005b. On incremental non-linearity in granular media: Phenomenological and multi-scale views (Part I). Int. J. Numer. Anal. Methods Geomech. 29 (14), 1387–1409. http://dx.doi.org/10.1002/nag.466.

Gao, Z., Zhao, J., 2017. A non-coaxial critical-state model for sand accounting for fabric anisotropy and fabric evolution. Int. J. Solids Struct. 106–107, 200–212. http://dx.doi.org/10.1016/j.ijsolstr.2016.11.019.

Gao, Z., Zhao, J., Li, X.-S., Dafalias, Y.F., 2014. A critical state sand plasticity model accounting for fabric evolution. Int. J. Numer. Anal. Methods Geomech. 38 (4), 370–390. http://dx.doi.org/10.1002/nag.2211.

Gu, X., Huang, M., Qian, J., 2014. DEM investigation on the evolution of microstructure in granular soils under shearing. Granul. Matter 16 (1), 91–106. http://dx.doi.org/10.1007/s10035-013-0467-z.

Hicher, P.Y., Chang, C.S., 2005. Evaluation of two homogenization techniques for modeling the elastic behavior of granular materials. J. Eng. Mech. 131 (11), 1184–1194. http://dx.doi.org/10.1061/(ASCE)0733-9399(2005)131:11(1184).

Hicher, P.Y., Chang, C.S., 2007. A microstructural elastoplastic model for unsaturated granular materials. Int. J. Solids Struct. 44 (7), 2304–2323. http://dx.doi.org/10.1016/j.ijsolstr.2006.07.007.

Hu, N., Zhuang, P.-Z., Yang, D.-S., Yu, H.-S., 2021. On the evolution law of a contact normal-based fabric tensor for granular materials. Comput. Geotech. 132, 103857. http://dx.doi.org/10.1016/j.compgeo.2020.103857.

Iyanaga, S., Kawada, Y., 1993. Encyclopedic Dictionary of Mathematics. Vol. 1, MIT Press.

Jenkins, J.T., 1988. Volume change in small strain axisymmetric deformations of a granular material. In: Satake, M., Jenkins, J.T. (Eds.), Studies in Applied Mechanics. In: Micromechanics of Granular Materials, vol. 20, Elsevier, pp. 245–252. http://dx.doi.org/10.1016/B978-0-444-70523-5.50035-7.

Li, X.S., Dafalias, Y.F., 2002. Constitutive modeling of inherently anisotropic sand behavior. J. Geotech. Geoenvironmental Eng. 128 (10), 868–880. http://dx.doi.org/10.1061/(ASCE)1090-0241(2002)128:10(868).

Li, X.S., Dafalias, Y.F., 2012. Anisotropic critical state theory: role of fabric. J. Eng. Mech. 138 (3), 263–275. http://dx.doi.org/10.1061/(ASCE)EM.1943-7889.0000324.

Liao, C.-L., Chang, T.-P., Young, D.-H., Chang, C.S., 1997. Stress-strain relationship for granular materials based on the hypothesis of best fit. Int. J. Solids Struct. 34 (31), 4087–4100. http://dx.doi.org/10.1016/S0020-7683(97)00015-2.

Love, A.E.H., 1927. A Treatise on the Mathematical Theory of Elasticity. University Press.

Nicot, F., Darve, F., 2011. The h-microdirectional model: accounting for a mesoscopic scale. Mech. Mater. 43 (12), 918–929. http://dx.doi.org/10.1016/j.mechmat.2011.07.006.

Nicot, F., Darve, F., RNVO Group: Natural Hazards and Vulnerability of Structures, 2005. A multi-scale approach to granular materials. Mech. Mater. 37 (9), 980–1006. http://dx.doi.org/10.1016/j.mechmat.2004.11.002.

Ouadfel, H., Rothenburg, L., 2001. 'Stress–force–fabric' relationship for assemblies of ellipsoids. Mech. Mater. 33 (4), 201–221. http://dx.doi.org/10.1016/S0167-6636(00)00057-0.

Papadimitriou, A.G., Chaloulos, Y.K., Dafalias, Y.F., 2019. A fabric-based sand plasticity model with reversal surfaces within anisotropic critical state theory. Acta Geotech. 14 (2), 253–277. http://dx.doi.org/10.1007/s11440-018-0751-5.

Petalas, A.L., Dafalias, Y.F., Papadimitriou, A.G., 2019. SANISAND-FN: an evolving fabric-based sand model accounting for stress principal axes rotation. Int. J. Numer. Anal. Methods Geomech. 43 (1), 97–123. http://dx.doi.org/10.1002/nag.2855.

Rothenburg, L., Bathurst, R.J., 1989. Analytical study of induced anisotropy in idealized granular materials. Géotech. 39 (4), 601–614. http://dx.doi.org/10.1680/geot.1989.39.4.601.

Suiker, A.S.J., Chang, C.S., 2004. Modeling failure and deformation of an assembly of spheres with frictional contacts. J. Eng. Mech. 130 (3), 283–293. http://dx.doi.org/10.1061/(ASCE)0733-9399(2004)130:3(283).

Sun, J., Sundaresan, S., 2011. A constitutive model with microstructure evolution for flow of rate-independent granular materials. J. Fluid Mech. 682, 590–616. http://dx.doi.org/10.1017/jfm.2011.251.

Tian, Y., Yao, Y.-P., 2018. Constitutive modeling of principal stress rotation by considering inherent and induced anisotropy of soils. Acta Geotech. 13 (6), 1299–1311. http://dx.doi.org/10.1007/s11440-018-0680-3.

Walton, K., 1987. The effective elastic moduli of a random packing of spheres. J. Mech. Phys. Solids 35 (2), 213–226. http://dx.doi.org/10.1016/0022-5096(87)90036-6.

Wan, R.G., Guo, J., 2001. Drained cyclic behavior of sand with fabric dependence. J. Eng. Mech. 127 (11), 1106–1116. http://dx.doi.org/10.1061/(ASCE)0733-9399(2001)127:11(1106).
Wan, R.G., Guo, P.J., 2004. Stress dilatancy and fabric dependencies on sand behavior. J. Eng. Mech. 130 (6), 635–645. http://dx.doi.org/10.1061/(ASCE)0733-9399(2004)130:6(635).
Wang, R., Dafalias, Y.F., Fu, P., Zhang, J.-M., 2020. Fabric evolution and dilatancy within anisotropic critical state theory guided and validated by DEM. Int. J. Solids Struct. 188–189, 210–222. http://dx.doi.org/10.1016/j.ijsolstr.2019.10.013.
Weber, J., 1966. Recherches concernant le contraintes intergranulaires dans les milieux pulvérents; applicationa la rhéologie de ces milieux. Cah. Fran c Cais Rhéol 2, 161–170.
Xiong, H., Nicot, F., Yin, Z.Y., 2017. A three-dimensional micromechanically based model. Int. J. Numer. Anal. Methods Geomech. 41 (17), 1669–1686. http://dx.doi.org/10.1002/nag.2692.
Yang, D., 2014. Microscopic Study of Granular Material Behaviours under General Stress Paths (Ph.D. thesis). University of Nottingham.
Yin, Z.-Y., Chang, C.S., 2009. Microstructural modelling of stress-dependent behaviour of clay. Int. J. Solids Struct. 46 (6), 1373–1388. http://dx.doi.org/10.1016/j.ijsolstr.2008.11.006.
Yin, Z.-Y., Chang, C.S., Hicher, P.-Y., 2010. Micromechanical modelling for effect of inherent anisotropy on cyclic behaviour of sand. Int. J. Solids Struct. 47 (14), 1933–1951. http://dx.doi.org/10.1016/j.ijsolstr.2010.03.028.
Yin, Z.-Y., Zhao, J., Hicher, P.-Y., 2014. A micromechanics-based model for sand-silt mixtures. Int. J. Solids Struct. 51 (6), 1350–1363. http://dx.doi.org/10.1016/j.ijsolstr.2013.12.027.
Zhao, C.-F., Kruyt, N.P., 2020. An evolution law for fabric anisotropy and its application in micromechanical modelling of granular materials. Int. J. Solids Struct. 196–197, 53–66. http://dx.doi.org/10.1016/j.ijsolstr.2020.04.007.
Zhao, C.-F., Salami, Y., Hicher, P.-Y., Yin, Z.-Y., 2019. Multiscale modeling of unsaturated granular materials based on thermodynamic principles. Contin. Mech. Thermodyn. 31 (1), 341–359. http://dx.doi.org/10.1007/s00161-018-0736-5.
Zhao, C., Salami, Y., Yin, Z.-Y., Hicher, P.-Y., 2017. A micromechanical model for unsaturated soils based on thermodynamics. In: Poromechanics VI. American Society of Civil Engineers, pp. 594–601. http://dx.doi.org/10.1061/9780784480779.073.
Zhao, C.-F., Yin, Z.-Y., Hicher, P.-Y., 2018a. Integrating a micromechanical model for multiscale analyses. Internat. J. Numer. Methods Engrg. 114 (2), 105–127. http://dx.doi.org/10.1002/nme.5735.
Zhao, C.-F., Yin, Z.-Y., Hicher, P.-Y., 2018b. A multiscale approach for investigating the effect of microstructural instability on global failure in granular materials. Int. J. Numer. Anal. Methods Geomech. 42 (17), 2065–2094. http://dx.doi.org/10.1002/nag.2842.